Journal of the European Ceramic Society 20 (2000) 235–244

Bauxite 'red mud' in the ceramic industry. Part 1: thermal behaviour

Vincenzo M. Sglavo [a,*], Renzo Campostrini [a], Stefano Maurina [a], Giovanni Carturan [a], Marzio Monagheddu [b], Gerolamo Budroni [b], Giorgio Cocco [b]

[a] *Dipartimento di Ingegneria dei Materiali, Universitá di Trento, Via Mesiano 77, I-38050 Trento, Italy*
[b] *Dipartimento di Chimica Fisica, Universitá di Sassari, Via Vienna 2, I-07100 Sassari, Italy*

Received 4 February 1999; accepted 22 March 1999

Abstract

Samples of red mud, by-products of alumina production from bauxite, are studied in the 120–1400°C interval. An extensive characterization was performed by thermal and X-ray diffraction analyses. The identification of gaseous species released upon heating was carried out by coupling the thermal analizer with a gas-chromatographic/mass spectrometer. Density evolution was also determined as a function of the heat treatment. Results indicate primary H_2O release from aluminium hydroxides, followed by carbonate decomposition with CO_2 evolution below 900°C. Alkaline oxides, mainly CaO and Na_2O, lead to the formation of $Ca_3Al_2O_6$ and $NaAlSiO_4$ between 900 and 1100°C. At the highest temperatures, reduction of Fe^{3+} to Fe^{2+}, involving O_2 release, promotes the formation of Fe_2TiO_4, with the disappearance of the rutile-TiO_2 phase. The various solid state reactions, ascertained at different stages of the heating process, and possible mass balances are discussed with reference to the state diagrams of principal red mud components.

Keywords: Bauxite; Red mud; Thermal analysis; Calcination; X-ray methods

1. Introduction

The activity of primary industries often yields substantial amounts of by-products. The disposal in the original industrial site is favoured by economic reasons — energy savings, transport, management and productivity — though traditional storage in nearby dumps can be impractical owing to the considerable masses involved and environmental restrictions. The local exploitation of these by-products is therefore a growing technological aspect of basic industries and one tenable option is their re-use as starting materials for other productions.

An emblematic case is the 'red mud' discharged by industry producing alumina from bauxite: alkaline digestion of 2.5 t of bauxite affords alumina and ≈1.5 t of red mud,[1–5] so that an average Al_2O_3 productivity of 5×10^5 t year^{-1} involves a mass of by-products of $\approx7.5\times10^5$ t year^{-1} discharged as slurry retaining variable water contents. This amount is composed of Fe and Ti oxides, behaving as chemically inert matter, with variable percentages of nominal SiO_2, Al_2O_3 and Na_2O. The material is available as a watery mixture which settles slowly and may easily be conveyed from station to station by continuous fluid-carrying machinery.

Several re-use plans have been advanced. Some fundamental studies concerning the extraction of single oxides — Fe_2O_3 or TiO_2 — are economically unsustainable.[2,3] As an example of possible applications requiring simple dewatering, we quote the use as acidic amender or bottom sealant (after stabilization with lime) in the construction of disposal sites.[2,6,7] The recycling of the mud, after curing or high temperature annealing — up to 1200°C — for large-rate daily mass consumption industries such as bricks and tile kilns has been put forward in a number of papers.[2,3,8–12]

Most of the above reports appear fragmentary and, to some extent surprising, characterization work is limited to the elemental analysis of the raw material and the identification of the crystalline phases in dried samples. However, the definition of thermal behaviour in a wide

* Corresponding author. Tel.: +39-0461-882468; Fax: +39-0461-881-977.
E-mail address: sglavo@ing.unitn.it (V.M. Sglavo).

0955-2219/00/$ - see front matter
PII: S0955-2219(99)00088-6

working range of temperatures appears mandatory for a feasible exploitation of the mud in high temperature applications. Indeed, the reactivity of red mud components on heating may promote ceramization and shrinkage and, apart from other qualities, may affect the mechanical features of clay-based items fabricated with bauxite-waste addition.

Accordingly, we focus here on the thermal behaviour of the mud, the solid-state transformations and solid–liquid phase transitions within the interval 120–1400°C. The use of thermal analysis coupled with a gas–mass spectrometry for detecting possible gas release, and of X-ray diffraction methods seemed well suitable for the problem at hand. The present study is a part of a long-term project on the exploitation of red mud as a clay additive for the ceramic industry or as a compound for self-binding mortars in the fabrication of stoneware. The results collected in this work regarding the evolution of various crystalline phases, occurrence of liquid phases and variations in colour will be used in the second part of the paper[13] more specifically addressed to technical aspects.

2. Experimental procedure

The red mud studied in this work was supplied by Eurallumina (Porto Vesme, Cagliari, Italy) as a mixture containing about 60% of solids, obtained immediately after alumina recovery from the digestion process. This material was heated for 2 h at 120°C, affording a reddish-orange powder.

Chemical analysis was performed by X-ray fluorescence (X' Unique II, Philips, The Netherlands).

Thermal analysis was performed on a Netzsch (Germany) STA 409 simultaneous analyser. Thermogravimetric (TG) and differential thermal (DT) analyses were performed in the range 20–1400°C (helium flow = 100 ml min^{-1}, heating rate = 10°C min^{-1}). Measurements were carried out in 0.3 cm^3 volume alumina crucibles using α-alumina as reference, analysing ≈100 mg of dry sample.

Mass spectrometric analysis was performed using a VG QMD 1000 quadrupole mass spectrometer (Carlo Erba, Italy). Mass spectra were obtained by electron impact at 70 eV with vacuum of $10^{-3.6}$ mbar and ionization chamber temperature equal to 200°C.

Thermogravimetric and mass spectrometric analyses were coupled according to a reported procedure.[14,15] Thermobalance and mass spectrometer were connected by a hollow silica glass column (length = 10 m, diameter = 0.32 mm) kept at 120°C permitting a continuous sampling of the gas phase released during the thermal treatment (scans from 3 to 400 amu every 0.9 s, delay time = 0.1 s). This allowed the record of the total ion current and of the ionic current of each m/z signal (m and z being the mass and the electrical charge of each ion, respectively) as a function of time/temperature.

Powder batches of about 50 g were treated for 8 h in air in the temperature interval 300–1400°C. A platinum crucible was used above 1200°C, owing to sample softening and the treated samples were subsequently milled to obtain a powder for successive analyses.

Density measurements were made with a helium picnometer (Micromeritics, Model 1305, USA).

X-ray diffraction (XRD) analysis was carried out on a Rigaku (Japan) D/MAX diffractometer (Cu$K\alpha$), equipped with a graphite monochromator in the diffracted beam. Crystalline phases were identified using the database of the International Center for Diffraction Data-JCPDS for inorganic substances.[16]

3. Results

The chemical composition of red mud dried at 120°C is reported in Table 1.

The thermogravimetric (TG) plot [Fig. 1(a)] shows a continuous weight loss distributed in the 100–1350°C interval. The high modulated trend of the TG derivative (DTG) curve [Fig. 1(b)] reveals the different contributions in detail: a broad band is centered at 140°C, followed by two intense peaks at 285 and 320°C and a plateau up to about 500°C (weight loss = 8.6%); a second, less pronounced weight loss, characterized by a plateau up to 680°C and a broad band centered at 835°C; a third range above 900°C with an evident signal at 1190°C (weight loss = 3.6%).

The DT curve [Fig. 1(a)] shows two small peaks: at 290°C, corresponding to the most intense peak of the DTG curve, and at 1250°C.

Three complementary pieces of information were gained from TG–MS experiments: (i) the presence of gaseous products evolved during the heat treatment, from the trend of the TIC curve; (ii) the chemical species released by the sample, from the recorded mass spectra; (iii) the relative abundance of gaseous species as a function of time, from the trend of the ion current corresponding to specific m/z signal.[14,15]

Table 1
Composition of red mud heated at 120°C (LOI = loss of ignition at 900°C): (a) wt%; (b) mol%

	Fe_2O_3	Al_2O_3	SiO_2	TiO_2	Na_2O	CaO	MgO	Cr_2O_3	P_2O_5	SO_3	ZrO_2	Cl	Other	LOI
(a)	35.2	20.0	11.6	9.2	7.5	6.7	0.4	0.4	0.3	0.3	0.3	0.2	0.6	7.3
(b)	22.2	19.8	19.5	11.6	12.2	12.0	1.0	0.3	0.2	0.4	0.3	0.6	–	–

The trend of TIC as a function of time/temperature (Fig. 2) shows features closely corresponding to those already observed in the DTG curve. The TIC curve is described by a first interval below 500°C with a broad band centered at 120°C, two strong sharp peaks at 290 and 320°C and two medium-intensity bands at 450 and 515°C. A second interval presents a plateau up to 675°C, two small bands and a broad band centered at 840°C. Above 900°C, the sharp signal at 1190°C presents an asymmetric shape and the TIC curve shows a modest increase up to the highest temperatures.

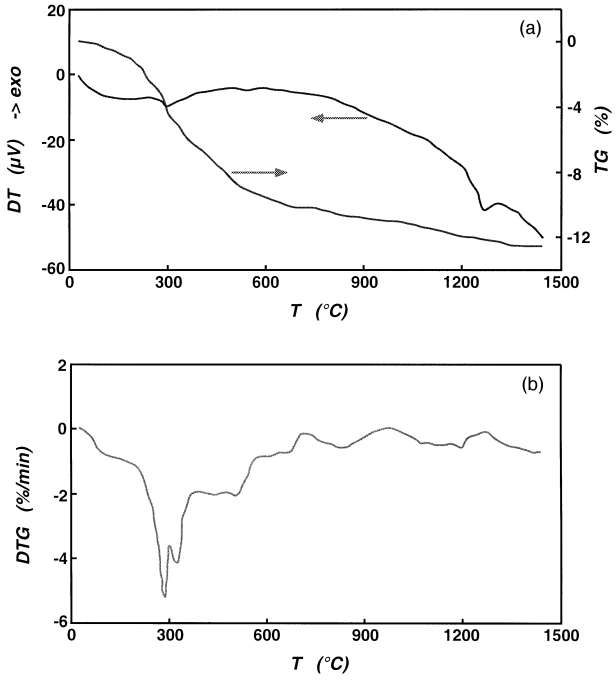

Fig. 1. (a) Thermogravimetric (TG) and differential thermal (DT) diagram of dried red mud; (b) derivative of TG curve (DTG).

The mass spectra recorded in correspondence of the TIC maxima below 675°C show the typical signals from H_2O (m/z = 18,17,16) and CO_2 (m/z = 44,28) only [Fig. 2(a)]. The TIC broad band at 840°C reveals the exclusive presence of CO_2 [Fig. 2(b)]. Spectra at the 1190°C TIC peak indicate the simultaneous evolution of SO_2 (m/z = 64, 66, 48, 50), O_2 (m/z = 32), HCl (m/z = 36, 38, 35) and traces of CO_2 [Fig. 2(c)]. The exclusive evolution of O_2 is recorded from the mass spectra at 1370°C [Fig. 2(d)].

Fig. 3 shows the ion current traces pertaining to the single chemical species evolved during the thermal treatment of red mud, namely H_2O, CO_2, SO_2, HCl and O_2.

Up to 320°C, H_2O evolution shows an ion current trend directly proportional to the TIC curve (Fig. 3); at higher temperatures a plateau up to 510°C is observed, whereas the final water release occurs below 720°C. The evolution of CO_2, detected by its molecular ion at m/z 44, is more complex owing to the contribution of four similar peaks: three partially overlapping signals, at 270, 480 and 670°C and the last at 840°C. HCl evolution presents a single broad peak at 1120°C. SO_2 evolution is described by a sharp peak at 1190°C. Molecular oxygen (m/z = 32) release starts at 1150°C with the first small

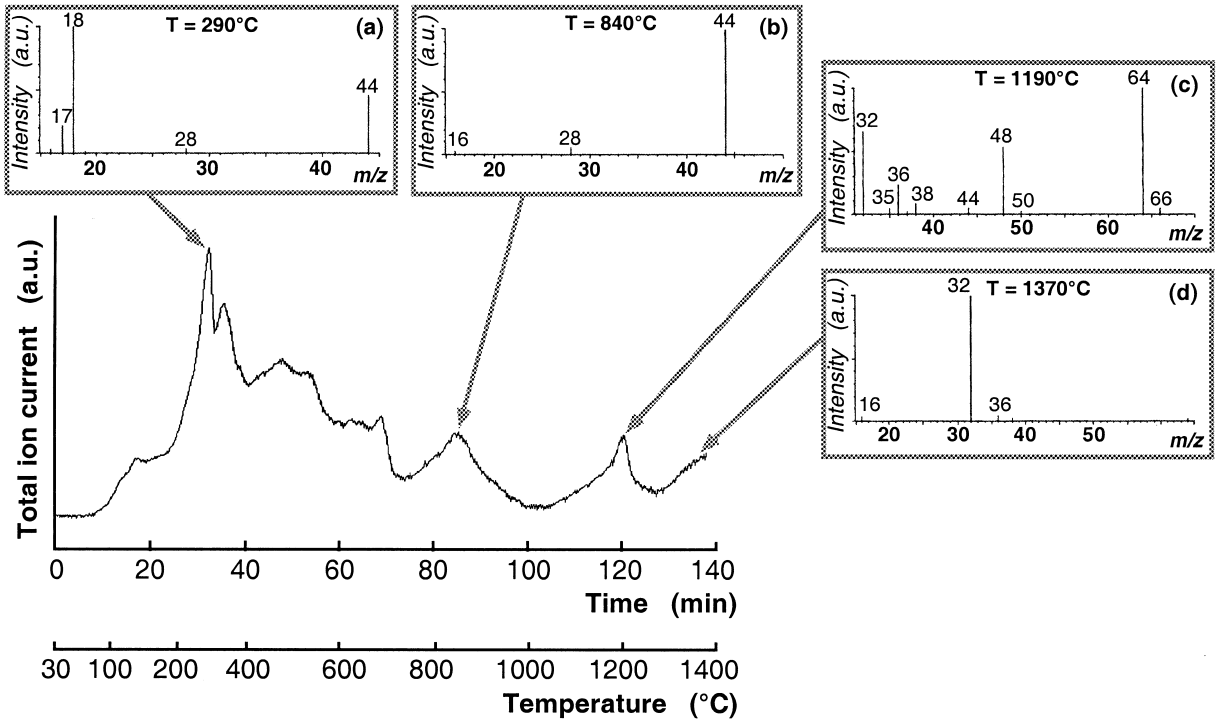

Fig. 2. Total ion current as a function of time and temperature. Mass spectra of the evolved gas mixtures at (a) 290, (b) 840, (c) 1190 and (d) 1370°C are reported in the insets.

band at 1190°C followed by a continuous increase with temperature. The TIC signal at the highest temperatures can be assigned to the evolution of oxygen molecules only.

The density change as a function of temperature is shown in Fig. 4: a decrease is observed up to 350°C, followed by a progressive increase, more pronounced between 900 and 1100°C.

Results concerning crystalline phases produced by heat treatment and identified by XRD analysis are summarized in Table 2. The number of crystalline phases in each sample is impressive: typical spectra are shown in Fig. 5.

Hematite constitutes the fundamental phase up to 1100°C. Above this temperature, the Hematite decrease parallels the occurrence of Fe_2TiO_4. TiO_2 is found as Rutile and Anatase below 800°C. Aluminum compounds show a sequence of phase transition: low-temperature hydroxides (Gibbsite, Bohmite and Bayerite) evolve with dehydration to χ-, η- and γ-Al_2O_3 below 900°C. γ-Al_2O_3 is observed at 1100°C. Above 900°C, corundum and θ-Al_2O_3 are the main aluminum oxide phases. Aluminium is also present in $Ca_{12}Al_{14}O_{33}$, $Na_{2x}Ca_{3-x}Al_2O_6$ and $Ca_3Al_2O_6$. Silicon oxide is always found in Quartz form. Hydroxy-silicate and two carbonate-silicates are present in the starting specimen dried at 120°C. These compounds decompose to $NaAlSiO_4$ (tricline) which affords Nepheline at 900°C. Two other $NaAlSiO_4$ phases, similar to nepheline, can be detected in samples treated at 1200°C. The presence of other Nepheline-like compounds of general formula $K_xNa_{4-x}Al_4O_{16}$ cannot be excluded. Minor components, such as $Na_2Si_2O_5$ and $Ca_3Fe_2Si_3O_{12}$, are detected at higher temperatures.

The colour evolution of samples fired in air is shown in Fig. 6. Red mud dried at 120°C appears orange–red. The colour turns dark red at 1000°C and brown at temperatures higher than 1200°C.

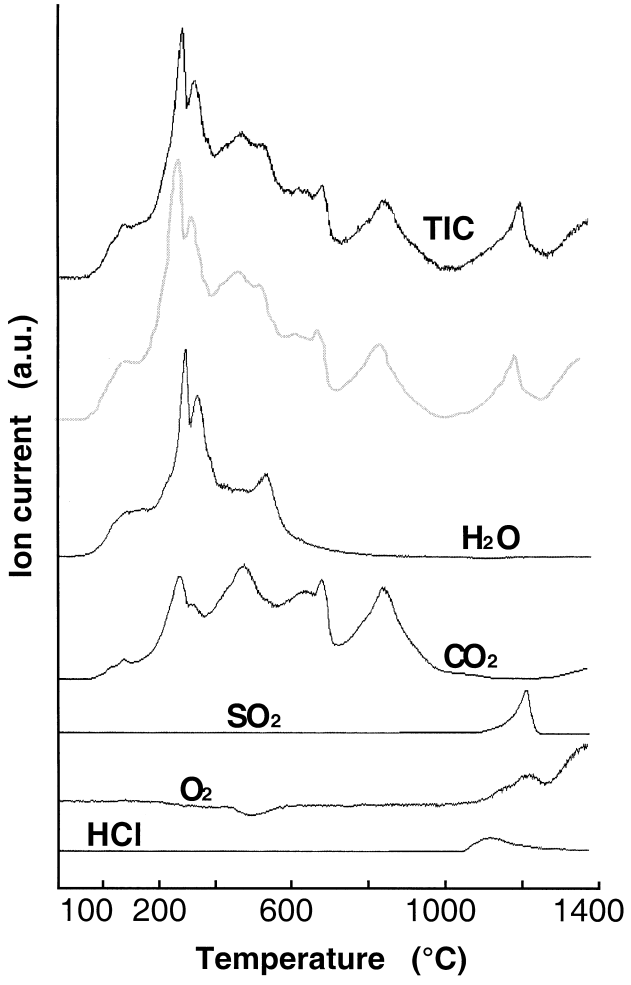

Fig. 3. Ion currents as a function of temperature for single gaseous species. Dashed curve corresponds to the total ion current reconstructed as the sum of the five single ion currents.

4. Discussion

The large amount of information resulting from the complementary techniques employed allowed a comprehensive view of the red mud behavior under heating.

As an introductory comment one notices a high reactivity essentially due to the extreme dispersion of red mud particles still observable in the powder dried at 120°C. Grain dimensions do not exceed 0.1 μm as shown in Fig. 7. This appears to be an ordinary feature of red mud obtained by alkaline digestion of bauxite, as observed in a number of cases.[8–10]

In the following sections, possible solid state reactions in the explored 120–1400°C range will be discussed referring to three main intervals identified by the thermal analysis: (i) up to 900°C, characterized by H_2O and CO_2 evolution, (ii) between 900 and 1100°C, where the thermal effects involve separation of CaO- and Na_2O-refractory phases and (iii) above 1100°C, a temperature range marked by Fe^{3+} reduction to Fe^{2+} with evolution of O_2.

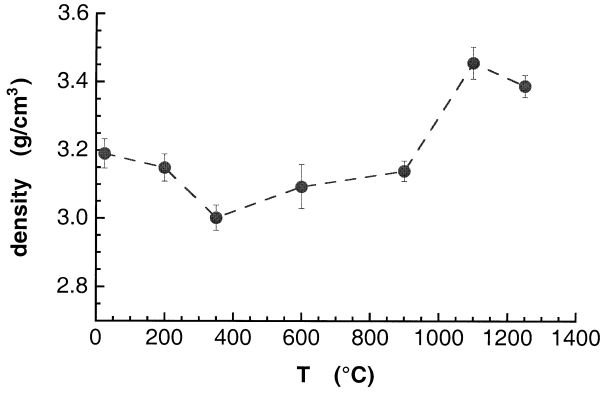

Fig. 4. Density evolution as a function of firing temperature.

Table 2
Crystalline phases detected by XRDA as a function of firing temperature. JCPDS[16] reference numbers are also reported

Dried in air		120°C		300°C		600°C		800°C		900°C	
Phases	JCPDS	Phases	JCPDS	Phases	JCPDS	Phases	JCPDS	Phases	JCPDS	Phases	JCPDS
Chantalite	29–1410	Chantalite	29–1410	Chantalite	29–1410	Cancrinite	34–176	$Na_5Al_3CSi_3)_{15}$	15–0469	$Ca_3Al_2O_6$	38–1429
Cancrinite	34–176	Cancrinite	34–176	Cancrinite	34–176	$Na_5Al_3CSi_3O_{15}$	15–0469	η-Al_2O_3	04–875	χ-Al_2O_3	13–373
$Na_5Al_3CSi_3O_{15}$	15–0469	$Na_5Al_3CSi_3O_{15}$	15–0469	$Na_5Al_3CSi_3O_{15}$	15–0469	η-Al_2O_3	04–875	χ-Al_2O_3	13–373	γ-Al_2O_3	29–63
Bayerite	20—11	Gibbsite	33–18	$\eta = Al_3O_3$	04–875	χ-Al_2O_3	13—373	γ-Al_2O_3	29–63	Hematite	33–664
Gibbsite	33–18	Bohmite	21–1307	χ-Al_2O_3	13–373	γ-Al_2O_3	29–63	Hermatite	33–664	Rutile	21–1276
Bohmite	21–1307	Hematite	33–664	Boymite	21–1307	Hematite	33–664	Rutile	21–1276	$NaAlSiO_4$	33–1203
Hematite	33–664	Rutile	21–1276	Hematite	33–664	Rutile	21–1276	Anatase	21–1272	Nepheline	35–424
Rutile	21–1276	Anatase	21–1272	Rutile	21–1276	Anatase	21–1272	Quartz	33–1161	Corundum	42–1468
Anatase	21–1272	Quartz	33–1161	Anatase	21–1272	Quartz	33–1161	$NaAlSiO_4$	33–1203	Quartz	33–1161
Quartz	33–1161	–	–	Quartz	33–1161	–	–	–	–	–	–

1000°C		1100°C		1200°C		1300°C		1400°C	
Phases	JCPDS	Phases	JCPDS	Phases	JCPDS	Phases	JCPDS	Phases	JCPDS
$Ca_3Al_2O_6$	38–1429	$Ca_3Al_2O_6$	38–1429	$Ca_3Al_2O_6$	38–1429	$Ca_3Al_2O_6$	385–1429	$Ca_3Al_2O_6$	38–1429
γ-Al_2O_3	29–63	γ-Al_2O_3	29–63	$Na_{2x}Ca_{3-x}Al_2O_6$	26–959	$Na_{2x}Ca_{3-x}Al_2O_6$	26–959	$Na_{2x}Ca_{3-x}Al_2O_6$	26–959
hermatite	33–664	Hermatite	33–664	Hematite	33–664	Hematite	33–664	Hematite	33–664
Rutile	21–1276	Rutile	21–1276	Ulvospinel	34–177	Ulvospinel	34–177	Ulvospinel	34–177
Nepheline	35–424	Nepheline	35–424	Andradite	10–288	Andradite	10–288	Andradite	10–288
Corundum	42–1468	Corundum	42–1468	Nepheline	35–424	Nepheline	35–424	Nepheline	35-424
θ-Al_2O_3	35–121	θ-Al_2O_3	35–121	$NaAlSiO_4$	33–1204	$(Na_2O)_{0.033}NaAISiO_4$	39–101	Corrundum	42–1468
Quartz	33–1161	Mayenite	09–413	Corundum	42–1468	Corundum	42—1468	θ-Al_2O_3	35–121
α-$Na_2Si_2O_5$	22–1397	α-$Na_2Si_2O_5$	22–1397	θ-Al_2O_3	35–121	θ-Al_2O_3	35–121	Mayenite	09–413
–	–	Quartz	33–1161	Mayenite	09–413	Mayenite	09–413	α-$Na_2Si_2O_5$	22–1397
–	–	–	–	α-$Na_2Si_2O_5$	22–1397	α-$Na_2Si_2O_5$	22–1397	Quartz	33–1161
–	–	–	–	Quartz	33–1161	Quartz	33–1161	–	–

For readers' benefit the results collected in Table 2 are summarized in a more significant form in the general Diagram 1. We also refer to Table 1 where the composition of the material heated up to 900°C is quoted as weight and mol percent.

4.1. Behaviour up to 800°C

Quartz and hematite are not affected by the heating process. The most important phenomenon is that of aluminium hydroxide transformations yielding η-, χ- and γ-Al_2O_3, accompanied by an endothermic peak in the DT curve [Fig. 1(a)]. $Al(OH)_3$ phases (Bayerite, Gibbsite and Bohmite), originated during bauxite chemical digestion,[17] evolve on heating similarly to sol–gel Al^{3+} materials which are involved in dehydration, together with solid-state topotactic transitions.[18–21] This tenable parallelism is further confirmed by the collapse to Corundum observed above 900°C; enjoying the highest stability and inertness, α-Al_2O_3 can be regarded as a

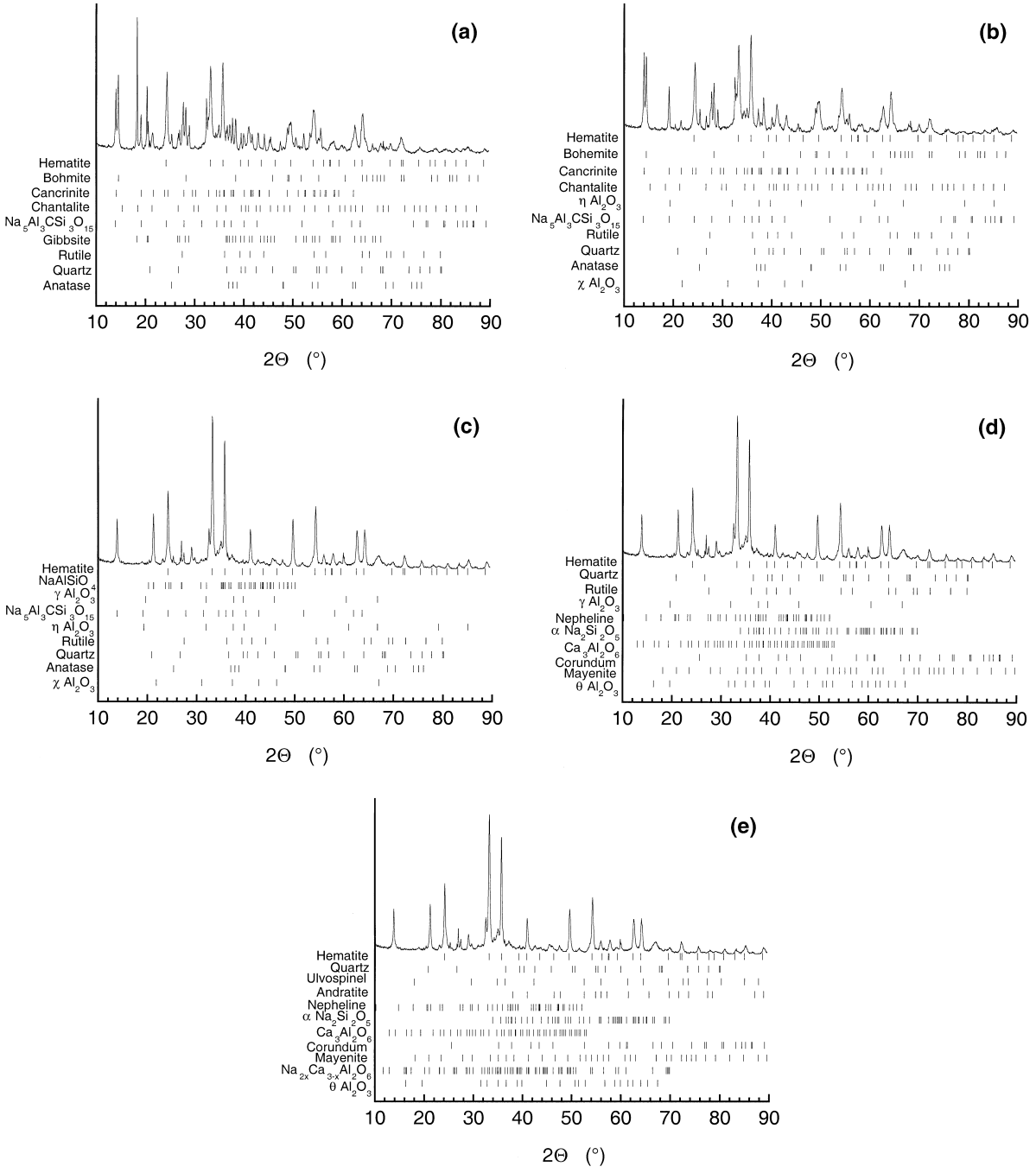

Fig. 5. XRD spectra recorded on (a) dried red mud and on samples heated at (b) 300, (c) 800, (d) 1100 and (e) 1400°C. Detected phases are also shown.

refractory product so that, in the temperature interval here considered, intermediate alumina phases should be considered as reactive species towards alkaline oxides. The TIC trend, almost completely attributed to H_2O evolution (Fig. 3), agrees with this interpretation. The trend of density as a function of temperature in the 120–600°C range (Fig. 4) may also be explained by Al^{3+} hydroxide dehydration, as aluminium oxide phases display densities ≈0.3 g cm^{-3} higher than bayerite, gibbsite and bohmite.[17,21]

In this temperature range TiO_2-anatase completely transforms into rutile as expected on the basis of TiO_2 state diagram.[22,23]

Decomposition of Chantalite, Cancrinite and $Na_5Al_3CSi_3O_{15}$ below 900°C corresponds to CO_2 evolution, as observed by TG–MS experiments (Fig. 3): the process produces definite amounts of alkaline oxides which are engaged by $NaAlSiO_4$ and incipient Nepheline.

4.2. Thermal effects between 900 and 1100°C

This temperature interval is dominated by the occurrence of Nepheline and $Ca_3Al_2O_6$. The Nepheline presence fits quite well with the decomposition of $Na_5Al_3CSi_3O_{15}$, Chantalite and Cancrinite. $NaAlSiO_4$ forms initially, while definite amounts of sodium silicate ($Na_2Si_2O_5$) are produced later at higher temperatures (≈1000°C), as expected from the state diagram. It is important to observe that the availability of Na_2O (12.1 mol%) exceeds the SiO_2 total content (19.3 mol%) potentially engaged in $NaAlSiO_4$ formation, thus revealing the presence of additional sodium oxide species not detected by XRD analyses. In addition, Nepheline occupies a definite field in the SiO_2–Al_2O_3–Na_2O state diagram[24] ultimately explaining the presence of these components as reactants in excess for a correct stoichiometric balance of reactions leading to $NaAlSiO_4$ and $Na_2Si_2O_5$.

The formation of Nepheline from Cancrinite determines the separation of CaO which is involved in the formation of $Ca_3Al_2O_6$:

$$3CaO + Al_2O_3 \rightarrow Ca_3Al_2O_6 \quad (1)$$

According to the Al_2O_3/CaO state diagram, an excess of CaO is required to form $Ca_3Al_2O_6$ by reaction (1). Considering the actual content of Al_2O_3 (19.8 mol%), a preventive total separation of CaO is needed for the subsequent reaction with Al_2O_3 resulting from hydroxides and aluminium carbonate-silicates decomposition. Only at higher temperatures (1100°C) Mayenite is formed as expected on the basis of the availability of CaO (12.0 mol%) and Al_2O_3 content.[25]

It is noteworthy that $Ca_3Al_2O_6$ displays a moderate setting character, with density of 3.04 g cm^3. The density increase from 600 to 1100°C (Fig. 4) may be due to the progressive formation of crystalline phases with higher densities (TiO_2-rutile 4.45 g cm^{-3}, γ-Al_2O_3 3.2 g cm^3, θ-Al_2O_3 3.56 g cm^3, nepheline 2.62 g cm^{-3}).[16]

An intriguing aspect of the thermal behaviour of this very reactive interval is the absence of $CaO/Al_2O_3/SiO_2$ and $CaO/Al_2O_3/Fe_2O_3$ ternary species. A possible

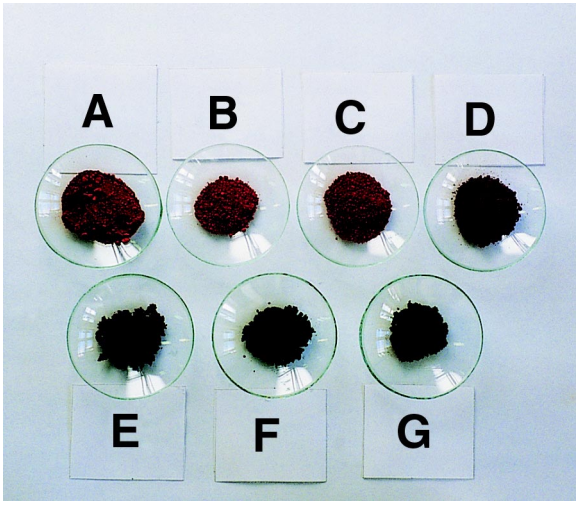

Fig. 6. Colour evolution of red mud fired at increasing temperatures: (a) 120, (b) 800, (c) 900, (d) 1000, (e) 1100, (f) 1200 and (g) 1400°C.

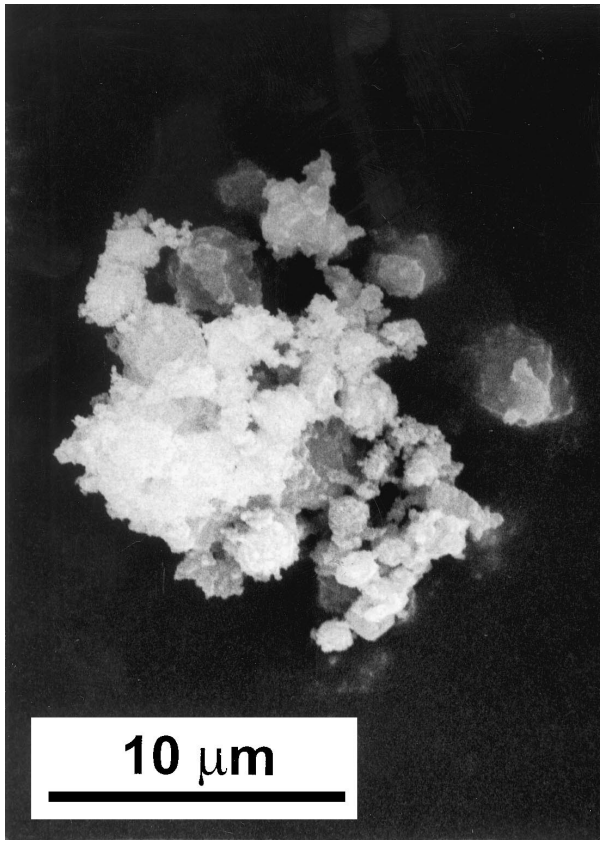

Fig. 7. Scanning electron micrograph of dried red mud particles.

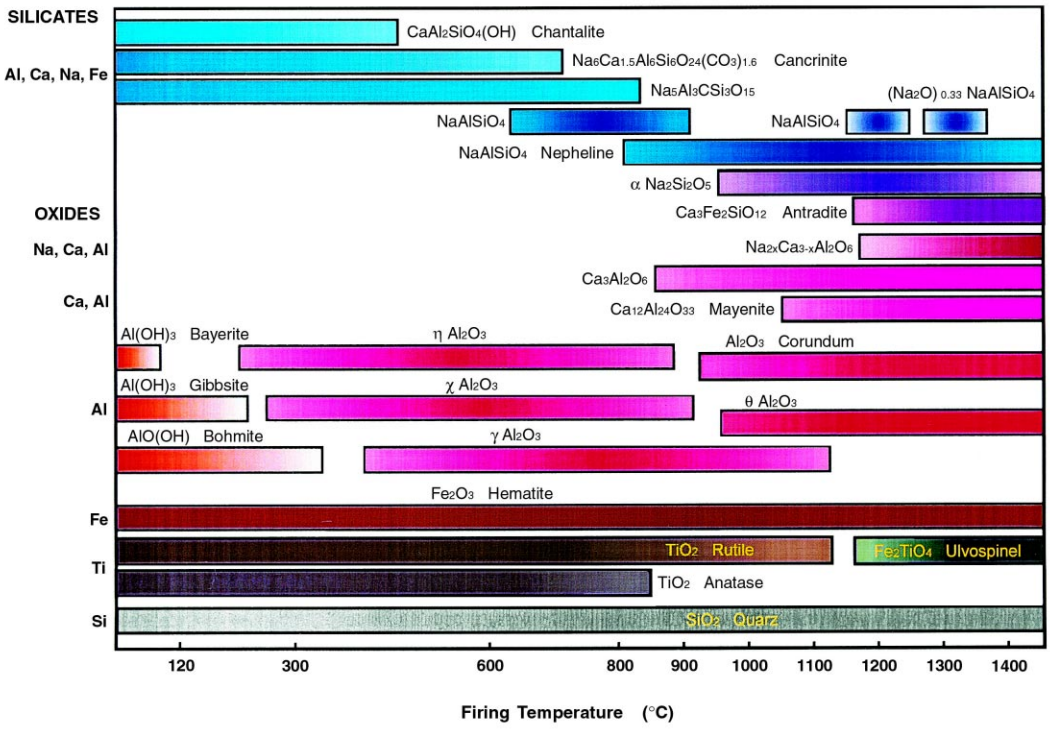

Diagram 1. Evolution of crystalline phases as a function of firing temperature

explanation may be advanced on the basis of the limited reactivity of α-Al_2O_3, Quartz and Hematite, so that the occurrence of $NaAlSiO_4$ and $Ca_3Al_2O_6$ should be ruled by the decomposition products of the aluminium–silicon carbonates.

In the present temperature range, the colour of red mud turns red–brown. This behaviour is related to the transformation of some white compounds (Bayerite and Gibbsite) into colourless phases such as $Ca_3Al_2O_6$ which causes the prevalence of the iron oxide (III) colour.[26]

4.3. Thermal transformations above 1100°C

Reduction of Fe^{3+} to Fe^{2+} characterizes thermal behaviour above 1100°C and promotes important chemical transformations. Hematite reduction to FeO is expected by Fe_2O_3/FeO state diagram[27–31] and is evidenced by molecular O_2 evolution in TG–MS results (Fig. 3). The absence of Fe_3O_4 is due to for by the formation of Ulvospinel Fe_2TiO_4, with immediate utilization of the entire TiO_2 load (11.5 mol%). The process occurs on the basis of the following reactions:

$$Fe_2O_3 \rightarrow 2FeO + 0.5O_2 \quad (2)$$

$$2FeO + TiO_2 \rightarrow Fe_2TiO_4 \quad (3)$$

Like the formation of $Ca_3Al_2O_6$ previously discussed, as only Ulvospinel is formed, reaction (3) must occur in excess of FeO.[29–31] In this temperature interval, iron oxide (III), not involved in reactions (2) and (3), reacts with CaO to produce andratite:

$$3CaO + Fe_2O_3 + 3SiO_2 \rightarrow Ca_3Fe_2Si_3O_{12} \quad (4)$$

As a matter of fact, some CaO becomes available, as part of the $Ca_3Al_2O_6$ either transforms into $Ca_{12}Al_{14}O_{33}$ according to:

$$7Ca_3Al_2O_6 \rightarrow Ca_{12}Al_{14}O_{33} + 9CaO \quad (5)$$

or reacts with Na_2O:

$$Ca_3Al_2O_6 + Na_2O \rightarrow Na_{2x}Ca_{3-x}Al_2O_6 + xCaO \quad (6)$$

It may be pointed out that the evolution of gaseous HCl and SO_2 recorded by TG–MS at 1100°C is related to the decomposition of alkaline salts, namely NaCl and Na_2SO_4, which make Na_2O available for reaction (6). Above 1200°C, the reactivity of crystalline components such as $Ca_3Al_2O_6$, Fe_2O_3 and SiO_2 is due to the presence of a well-developed liquid phase, mainly composed by Nepheline and sodium silicate.

The presence of definite amounts of $Na_2Si_2O_5$ and nepheline accounts for the record of a *solidus–liquidus* transformation in the DT plot ($T = 1219$°C; Fig. 1) which is also related to the softening of the red mud powder observed above 1200°C. This effect, connected to the evolution of gaseous species, namely O_2, HCl and SO_2, can be used to define a temperature upper limit for

some applications which require the maintainance of the initial shape of the body.

The density decrease observed above 1100°C (Fig. 4) reflects the occurrence of ulvospinel (density $=4.79$ g cm^3) and andratite (density $=3.86$ g cm^{-3}) from hematite (density $=5.27$ g cm^{-3}).[16] This decrease is partly compensated by the increase in corundum (density $=3.99$ g cm^{-3}) from low-density alumina phases.[17]

Thermal effects above 1100°C are visually indicated by a definite change in colour which turns from red to brown (Fig. 6). This phenomenon is associated with the Fe^{3+} (3d5, high-spin electronic configuration) reduction to Fe^{2+} (3d6) in Ulvospinel (dark grey[16]), allowing photonic absorptions at lower energy.

5. Conclusions

The thermal evolution of bauxite-derived red mud was studied in this work by different complementary techniques. Dried red mud is substantially inert up to 900°C, the loss of H_2O from aluminium hydroxides and of CO_2 from silico-alumino-carbonates being the only detectable effects. At 900°C red mud is dark red in colour. In the 900–1100°C interval, samples are involved in the formation of Nepheline and $Na_2Si_2O_5$ which are responsible for the softening of samples at ≈1200°C. Fundamental components (Fe_2O_3 and TiO_2, ≈50% of the original mass) maintain their original state. Fe_2O_3 and TiO_2 are reagents for Fe_2TiO_4 occurrence with O_2 evolution above 1100°C. This reaction is responsible for the brown colour observed above 1200°C.

The obtained results represent a fundamental starting point for any re-use of red mud as raw material for the ceramic industry. The moderate reactivity up to 900°C makes the red mud useful as an inert component in the fabrication of traditional clay-based ceramics, such as tiles or bricks, which are usually fired at temperatures lower than 1000°C. In this case, the red colour and the extremely fine particle size of the mud represent an interesting factor. At higher temperatures, red mud can constitute the source of low melting point sodium silicates thus promoting liquid phase sintering in ceramic bodies which can result in higher strength and lower porosity. Also in this case, depending on the firing temperature, different colour gradations can be produced.

Acknowledgements

This work was supported by EMSA (Cagliari, Italy) under Contract EMSA-INCM 'Riutilizzo di fanghi rossi'. The authors would like to thank Miss Alexia Conci for the contribution in the experimental work. Dr. Ullu (EMSA, Cagliari, Italy) and Dr. Teodosi (Eurallumina, Porto Vesme, Cagliari, Italy) are also acknowledged for their collaboration.

References

1. Bayer, G., Möglichkeiten zur Wirtschaftlichen Beseitigung von Rotschlämmen. *Erzmetall*., 1972, **25**(9), 454–457 (in German).
2. Parek, B. K. and Goldberger, W., An assessment of technology for possible utilization of bayer process muds, Battelle Columbus Labs Report no. EPA-600/2-76-301, Columbus, OH, 1976.
3. Di San Filippo, A., *Riutilizzo del Fango Rosso, Rendiconti del Seminario della Facoltá di Scienze dell'Universitá di Cagliari*, Vol. L (3–4). Sigla Esse, Cagliari, Italy, 1980 (in Italian).
4. Haake, G., Rotschlamm—Abfall oder Verwertbares Nebenprodukt? Neue Hutte, 1988, **33**(11), 424–429 (in German).
5. Musselman, L. L., Production processes, properties and applications for aluminum-containing hydroxides. In *Alumina Chemicals: Science and Technology Handbook*, ed. L. D. Hart. The American Ceramic Society, Columbus, OH, USA, 1990, pp. 75–92.
6. Lotze, J. and Wargalla, G., Rotschlamm—Ein Baustoff zur Deponie-Basisabdichtung. *Erzmetall*., 1986, **39**(7–8), 394–398 (in German).
7. Browner, R. E., The use of bauxite waste mud in the heap leaching of gold ores. *Minerals and Metallurgical Processing*, 1992 February, 48–50.
8. Tauber, T., Hill, R. K., Crook, D. N. and Murray, M. J., Red mud residues from alumina production as a raw material for heavy clay products. *J. Austr. Ceram. Soc*., 1971, **7**(1), 12–17.
9. Knight, J. C., Wagh, A. S. and Reid, W. A., The mechanical properties of ceramics from bauxite waste. *J. Mater. Sci*., 1986, **21**, 2179–2184.
10. Wagh, A. S. and Douse, V. E., Silicate bonded unsintered ceramics of Bayer process waste. *J. Mater. Res*., 1991, **6**(5), 1094–1102.
11. Wagh, A. S. and Douse, V. E., Silicate bonding of laterites—an ancient process for construction components. In *Ceramics and Civilization, Vol. VI, The Social and Cultural Contexts of New Ceramic Technologies*, ed. W. D. Kingery. The American Ceramic Society, Westerville, OH, 1993, pp. 75–87.
12. Kara, M. and Emrullahoglu, Ö. F., Study of Seydisehir red mud wastes as brick and roofing tiles. In *Fourth Euroceramics*, Vol. 12, ed. I. Braga, S, Cavallini and G. F. Di Cesare. Faenza Editrice, Faenza, Italy, 1995, pp. 155–162.
13. Sglavo, V. M., Maurina, S., Conci, A., Salviati, A., Carturan and Cocco, G., Bauxite "red mud" in the ceramic industry. Part 2: production of clay-based ceramics. *J. Eur. Ceram. Soc*. accepted for publication.
14. Marci, G., Palmisano, L., Sclafani, A., Venezia, A. M., Campostrini, R., Carturan, G., Martin, C., Rives, V. and Solana, G., Influence of tungsten oxide on structural and surface properties of sol-gel prepared TiO_2 employed for 4-nitrophenol photodegradation. *J. Chem. Soc., Faraday Trans*., 1996, **92**(5), 819–829.
15. Campostrini, R., D'Andrea, G., Carturan, G., Ceccato, R. and Sorarú, G. D., Pyrolisis study on methyl-substituted Si-H containing gels as precursors for oxycarbide glasses, by combined thermogravimetry, gas chromatographic and mass spectrometric analysis. *J. Mater. Chem*., 1996, **6**(4), 585–594.
16. JCPDS, International Centre for Diffraction Data, 1601 Park Line, Swarthmore, PA, 1987.
17. Wefers, K., Nomenclature, preparation and pProperties of aluminum oxides, oxide hydroxides and trihydroxides. In *Alumina Chemicals: Science and Technology Handbook*, ed. L. D. Hart. The American Ceramic Society, Columbus, OH, 1990, pp. 13–22.
18. Mariotto, G., Cazzanelli, E., Carturan, G., Di Maggio, R. and Scardi, P., Raman and X-ray diffraction study of boehmite gels and their transformation to α- and γ-alumina. *J. Solid State Chem*., 1990, **86**, 263–274.

19. Carturan, G., Di Maggio, R., Montagna, M., Pilla, O. and Scardi, P., Kinetics of phase separation and thermal behaviour of gel-derived Al_2O_3 doped by Cr_2O_3: an X-ray diffraction and fluorescence spectroscopy study. *J. Mater. Sci.*, 1990, **25**, 2705–2710.
20. Pach, L., Roy, R. and Kormaneni, S., Nucleation of alpha alumina in boehmite gel. *J. Mater. Res.*, 1990, **5**(2), 278–285.
21. Levin, I. and Brandon, D., Metastable alumina polimorphs: crystal structures and transition sequences. *J. Am. Ceram. Soc.*, 1998, **81**(8), 1995–2012.
22. The American Ceramic Society (eds), *Phase Diagrams for Ceramists*, (1975 Supplement). The American Ceramic Society, Columbus, OH, 1975.
23. Cocco, G., Campostrini, R., Cabras, M. A. and Carturan, G., Propene hydrogenation on low-temperature reduced Pt/TiO_2 phases and H_2 treatment on specific catalytic Activity. *J. Mol. Catal.*, 1994, **94**, 299–310.
24. The American Ceramic Society (eds), Phase diagrams for ceramists, Vol. I. The American Ceramic Society, Columbus, OH, 1964, p. 181.
25. The American Ceramic Society (eds), Phase Diagrams for Ceramists, Vol. IV, The American Ceramic Society, Columbus, OH, 1981, p. 95.
26. Cornell, R. M. and Schwertmann, U., *The Iron Oxide*. VCH, New York, 1996, pp.180–187.
27. The American Ceramic Society (eds), *Phase Diagrams for Ceramists*, Vol. I. The American Ceramic Society, Columbus, OH, 1964, pp. 38–39.
28. Benard, J., Michel, A., Philibert, J. and Tablet, J., *Metallurgie Generale*, 2nd edn. Masson, Paris, 1984 pp. 471–81 (in French).
29. Cornell, R. M. and Schwertmann, U., *The Iron Oxide*. VCH, New York, 1996, p. 377.
30. The American Ceramic Society (eds), *Phase Diagrams for Ceramists*, Vol. I. The American Ceramic Society, Columbus, OH, 1964, pp. 62–63.
31. The American Ceramic Society (eds), *Phase Diagrams for Ceramists*, Vol. II. The American Ceramic Society, Columbus, OH, 1964, pp. 40–41.